



Site-selective doping mechanisms for the enhanced photocatalytic activity of tin oxide nanoparticles

Woo-Sung Jang^{a,b,1}, Yeongrok Jin^{c,1}, Young-Hoon Kim^{a,1}, Sang-Hyeok Yang^a, Seon Je Kim^a, Jung A. Hong^a, Jaeyoon Baik^e, Jaekwang Lee^{c,*}, Hangil Lee^{d,*}, Young-Min Kim^{a,b,**}

^a Department of Energy Science, Sungkyunkwan University (SKKU), Suwon 16419, Republic of Korea

^b Center for Integrated Nanostructure Physics, Institute for Basic Science (IBS), Suwon 16419, Republic of Korea

^c Department of Physics, Pusan National University, Busan 46241, Republic of Korea

^d Department of Chemistry, Sookmyung Women's University, Seoul 04310, Republic of Korea

^e Beamline Research Division, Pohang Accelerator Laboratory (PAL), Pohang 790-784, Republic of Korea

ARTICLE INFO

Keywords:

Metal oxide nanoparticle

Doping

Atomic defect

Oxygen vacancy

Lattice strain

ABSTRACT

The addition of transition metal dopants into metal oxide nanoparticles (MO NPs) is an universal strategy to engineer the electronic and chemical properties of NPs. Although doping phenomena strongly rely on interactions with compositional and electronic degrees of freedom, fully understanding the site-specific doping behavior in the lattice framework of MO NP on atomic scale remains challenging. Here, we directly resolve the atomic site-selective (substitutional or interstitial) doping behaviors of Cr and Fe in SnO₂, revealing their different roles in photocatalytic activities. Atomic-resolution microscopy combined with spectroscopy reveals two contrasting doping behaviors: Cr³⁺ substitutes for Sn⁴⁺ associated with the formation of oxygen vacancies, whereas Fe³⁺ occupies interstitial sites accompanied by lattice strain. Theoretical calculations indicate that substitutional dopant-vacancy cooperation and interstitial dopant-strain coupling can be energetically favorable routes for enhancing catalytic properties. Our results provide fundamental insights into atomic-scale doping mechanisms and engineering strategies for high-performance doped MO NPs.

1. Introduction

Metal oxide nanoparticles (MO NPs) display catalytic properties similar to those of metal catalysts and thus have been used as photocatalysts with various geometrical forms and different sizes and shapes for several decades [1–3]. Nonetheless, there is an ongoing need for reliable and efficient methods that harvest energy from the whole solar spectrum, including visible light. Thus, advanced catalyst materials are of great importance, and conventional catalyst materials should be improved by a facilely adoptable, mass-producible, economic, and reliable method for obtaining visible-light photocatalysts [4–9].

Metal or cation doping on photocatalytic NPs has been widely adopted as an effective approach to altering or improving electronic, optical, magnetic, and catalytic properties with a focus on increasing the local charge imbalance by intentionally introducing excess electrons or holes. These active catalytic sites associated with atomic defects and

excess charges at the surface promote chemical reactions [10]. This simple ionic scenario considering charge compensation, in combination with the perspectives of local strain (related to ionic radius) and defect density (related to surface area), has typically explained the enhanced photocatalytic properties of doped MO NPs. However, the physical properties of doped MO NPs depend on the very complicated interplay among lattice strain, chemical states, charges, and site occupancies of defects, and the resulting ramifications are significant for even extremely low concentrations of dopants [11,12]. Thus, precise information on the site selectivity of dopants in the host lattice is required for a fundamental understanding of the underlying catalytic mechanism at an atomic level.

To address this issue, we combined advanced scanning transmission electron microscopy (STEM) with multiscale and multimodal spectroscopic approaches and density functional theory (DFT) calculations, by which the site selectivity and chemical states of transition metal (TM)

* Corresponding authors.

** Corresponding author at: Department of Energy Science, Sungkyunkwan University (SKKU), Suwon 16419, Republic of Korea.

E-mail addresses: jaekwangl@pusan.ac.kr (J. Lee), easyscan@sookmyung.ac.kr (H. Lee), youngmk@skku.edu (Y.-M. Kim).

¹ Equal contribution.

dopants in MO NPs were resolved and investigated at the atomic scale. As a model system, we chose SnO₂ NPs doped with the TMs, Cr and Fe, which have been demonstrated to be useful candidates that can effectively improve the photocatalytic activity and maintain structural stability after doping [13–15]. SnO₂ has been considered as one of the best smart materials and has a wide range of applications, such as solar cells [16,17], photocatalyst supports [18,19], and chemical sensors [20,21]. However, it has a large bandgap, which is a drawback that limits its usability in the visible region. From an engineering perspective, doping TMs into SnO₂ has been widely used as a facile means of tackling this issue. Presumably, the trivalent dopants Cr and Fe form ionic defects that substitute for tetravalent Sn sites accompanied by the formation of oxygen vacancies (V_O) [22,23]. Considering the ionic radii of Cr³⁺ (0.615 Å) and Fe³⁺ (0.645 Å) coordinated with six oxygens and that of six-coordinated Sn⁴⁺ (0.69 Å) [24], the previous interpretations appear reasonable because the ionic radii of the TMs are comparable to that of the host cation [25] and because the resulting photocatalytic improvements obtained by the doping of the two TMs are similar to one another. However, direct observation and probing of the site-specific doping behavior of TMs in MO NPs have rarely been successful.

In this study, the two contrasting doping behaviors of Cr and Fe TMs into SnO₂ NPs are first resolved at the atomic scale: substitutional doping of Cr and interstitial doping of Fe with the same valency of +3. Intriguingly, the Fe interstitials are associated with the lattice strain of the SnO₂ rutile structure, while the Cr substitutes incur a high density of V_O for charge compensation. Theoretical calculations indicate that Cr³⁺ prefers substitutional sites rather than interstitial sites, whereas Fe³⁺ shows the opposite trend. Relative to that in pristine SnO₂, the V_O formation energy is revealed to be much lower near substitutional Cr atoms in SnO₂ but substantially higher near interstitial Fe atoms; thus, the V_O density is notably suppressed by Fe doping. Our combined approach directly reveals the two contrasting doping behaviors of substitutional TM–V_O cooperation and interstitial TM–strain coupling in SnO₂ NPs, suggesting that the microscopic mechanisms for the improvement of photocatalytic properties are intrinsically different depending on the type of TM, even if the TMs under consideration are similar in ionic size and valency. The implications of this study emphasize the importance of microscopy-based direct observation for obtaining a fundamental understanding of the doping effect occurring at the atomic scale.

2. Experimental

2.1. Preparation of TM-doped SnO₂ NPs

We prepared precursor solutions using one-pot syntheses. A total of 10 mmol of tin(IV) chloride pentahydrate (SnCl₄·5H₂O, 98%) was added to 10 mL of 2-methoxy ethanol (≥ 99.9%). The dopants (TM = Fe or Cr) were added in the form of hydrated transition metal nitrates (TM (NO₃)_x·nH₂O) in the desired amounts determined by calculating the mole fraction of the metal dopant according to the equation (moles of TM)/[(moles of TM) + (moles of Sn)]. After approximately 10 min, the synthetic gel solution became transparent. Then, the solutions were transferred to Teflon-lined autoclaves, which were sealed and heated at 220 °C for 7 h in a convection oven. After the synthesis of 5 mol% TM-doped SnO₂ NPs, the three types of NPs (pristine, Fe-doped, and Cr-doped SnO₂ NPs) were annealed at 300 °C for 12 h. The three tested NPs were then obtained. 4-Chlorophenol (99.0% purity) was purchased from Sigma–Aldrich.

2.2. Characterizations

To examine the photocatalytic activity, the three tested NPs (0.5 g/L) containing 4-chlorophenol (100 μL) were stirred in the dark for 10 min until adsorption equilibrium was reached before UV illumination. The reactor was illuminated by a 300 W Xe arc lamp (Newport) with moderate continuous stirring (80 rpm). The light was passed through a cutoff

filter (λ ≥ 320 nm) and then focused on the center of the reactor. During the process, 1 mL of the suspension was withdrawn at set time intervals, and the TM-doped SnO₂ NP residue was separated by a 0.45-μm Whatman filter. The atomic structures of the NPs were acquired by aberration-corrected scanning transmission electron microscopy (STEM) in high-angle annular dark field (HAADF) imaging mode at an accelerating voltage of 200 kV (JEM-ARM200CF, JEOL). The collection angle range of the ADF detector was 68–280 mrad, and the probe forming angle was approximately 23 mrad. Random background noise in the ADF-STEM images was reduced using the Wiener filtering method implemented in a commercial program (HREM Filter Pro, HREM Research Ltd.). All the simulated images were obtained by the use of the QSTEM software package with microscope defocus of Δf = +10 nm using an aberration-corrected probe with C_s = −0.037 μm and a probe-forming aperture of 23 mrad at an accelerating voltage of 200 kV; these parameters were chosen to approximate the experimental conditions. The nanoscale elemental mapping of Fe-doped SnO₂ and Cr-doped SnO₂ NPs was performed using energy dispersive X-ray spectroscopy (EDX) in the same ADF-STEM imaging mode with a dual-type silicon drift detector (JED-2300T, JEOL Ltd.) with a large effective solid angle (ca. 1.2 sr.). Each detector has an effective X-ray sensing area of 100 mm², providing a collection efficiency of up to ca. 10% of the total X-ray signal (4π sr.). To complement the elemental mapping, electron energy loss spectroscopy (EELS, Gatan GIF Quantum ER 965) of the NPs in the same ADF-STEM imaging mode was carried out to obtain core-loss EELS spectra of the O K-edge, Fe L-edge, and Cr L-edge. XRD patterns of the TM-doped SnO₂ NPs were obtained using Ni-filtered Cu-K_α radiation and a Rigaku D/Max-A diffractometer. Scanning transmission X-ray microscopy (STXM) was performed at the 10A1 beamline of the Pohang Accelerator Laboratory (PAL). Image stacks were acquired using X-ray absorption spectroscopy (XAS) to extract the Sn M₅-edge spectra.

2.3. DFT calculations

In this work, the structural and electronic properties of TM-doped SnO₂ crystals and surfaces were studied from first principles in the framework of DFT. The TM-doped SnO₂ systems were modeled using 48-atom 2 × 2 × 2 supercells for the formation energy calculations and 180-atom slabs of stoichiometric SnO₂ with (110) surfaces consisting of five Sn–O layers for the density of states (DOS) calculations, with a single dopant of substitutional (or interstitial) Fe (or Cr). The projector augmented wave (PAW) [26] pseudopotentials were used to treat electron-ion interactions, and the generalized gradient approximation (GGA) parametrized by the Perdew–Burke–Ernzerhof (PBE) [27]-based hybrid functional (PBE0) [27] was used to describe the electron exchange–correlation interactions. The DOS for each optimized doped SnO₂ slab structure was calculated using the tetrahedron method with Blöchl corrections [26]. A 450 eV cutoff energy for the plane wave basis set was used. 2 × 2 × 3 and 2 × 2 × 1 Γ-centered *k*-point meshes were used for the 2 × 2 × 2 supercells and for the slab structures, respectively. The calculations were converged in energy to 10^{−6} eV/cell, and the structures were allowed to relax until the forces were less than 10^{−2} eV/Å. All spin-polarized calculations were carried out using the Vienna *Ab-initio* Simulation Package (VASP) [28]. The formation energy of defects ($E_{\text{form}}^{\text{X}}$) was calculated using the following relation:

$$E_{\text{form}}^{\text{X}} = E_{\text{doped}}^{\text{X}} - E_{\text{undoped}} - n\mu_{\text{X}} - m\mu_{\text{Sn}}$$

where $E_{\text{doped}}^{\text{X}}$ is the total energy of a 2 × 2 × 2 supercell of SnO₂ containing defect X (X = Fe and Cr) and a 2 × 3 SnO₂ (110) slab of 5 at. layers with defect X (X = O), E_{undoped} is the total energy of a 2 × 2 × 2 supercell of undoped SnO₂ and a 2 × 3 SnO₂ (110) slab of 5 at. layers, *n* is the number of defects X, μ_{X} is the chemical potential of defect X, *m* is the number of Sn atoms, and μ_{Sn} is the chemical potential of Sn. To obtain O K edge X-ray absorption near-edge spectroscopy (XANES)

spectra of SnO_{2-x} , the dielectric function was calculated using the supercell core-hole (SCH) method [29]. The following imaginary part of the dielectric function in the long wavelength limit ($q = 0$) is directly proportional to the absorption spectrum:

$$\epsilon_{\text{af}}^{(2)}(\omega) = \frac{4\pi^2 e^2 \hbar^4}{\Omega \omega^2 m_e^2} \sum_{c,k} 2\omega_k \delta(\epsilon_{ck} - \epsilon_{\text{core}} - \omega) \times M_{\alpha}^{\text{core} \rightarrow ck} M_{\beta}^{\text{core} \rightarrow ck*}$$

3. Results and discussion

3.1. Nanoscale characterizations and photocatalytic property of doped SnO_2 NPs

Pristine, Cr-doped, and Fe-doped SnO_2 NPs were prepared using a one-pot synthesis method (see details in Methods). Fig. 1a–c shows bright-field (BF) STEM images of the pristine, Cr-doped, and Fe-doped SnO_2 NPs after annealing at 300 °C for 12 h. The average particle size of the three samples was estimated to be in the range of ~7–10 nm (see insets in Fig. 1a–c), and the value tended to slightly decrease after doping with Cr and Fe. This size reduction would contribute to improvements in the resulting photocatalytic properties to some extent but not substantially. To confirm TM doping into the SnO_2 NPs, nanoscale elemental mapping of the three samples was performed using STEM-based energy dispersive X-ray spectroscopy (EDX) (Fig. 1d–g). The results show that the two dopants Cr and Fe seem to be evenly distributed in the SnO_2 NPs without segregation or the formation of byproducts. The photocatalytic performance of the three samples was assessed by monitoring the decomposition of 4-chlorophenol (4-CP) in aerated aqueous suspensions of SnO_2 upon illumination with near-UV light for 3 h (Fig. 1h). The photocatalytic degradation (PCD) rate of 4-CP is ~1.6 times faster in doped SnO_2 than in pristine SnO_2 . The superior PCD

properties of the doped SnO_2 NPs were demonstrated to be well sustained after five re-uses, which suggests the robustness of the photocatalytic properties of the doped SnO_2 NPs in cyclic use and their practical applicability (Fig. S1).

Aside from the minor contribution of size reduction, it is surmised that the notable property improvement in doped SnO_2 originates from atomic-level structural and electronic modifications by the foreign dopants near the surface. Then, the following question naturally arises regarding the roles of these dopants in enhancing physical properties: Do they play a similar role at the quantum level?

3.2. Atomic structures of Cr- and Fe-doped SnO_2 NPs

To explore the atomic site-specific doping behaviors of the two TMs Cr and Fe in SnO_2 NPs, the atomic structures of SnO_2 NPs doped with Cr and Fe were captured using high-angle annular dark field (HAADF) and annular bright field (ABF) STEM imaging. The HAADF mode is relatively insensitive to the local tilt of the sample, and its contrast is roughly scaled to the squared atomic number (Z^2) [12,31,32], while the ABF mode can effectively collect the weakly scattered signal of a low-Z element such as oxygen or a low-concentration dopant [33]. Thus, HAADF STEM was employed to image the lattice framework of Sn cations to measure the local lattice distortion, and ABF STEM was used to image the overall crystal structures of the three samples, including the positions of elements. Fig. 2a–c shows the lattice structures of [001]-oriented pristine, Cr-doped, and Fe-doped SnO_2 NPs. The results confirm that the structures of the two doped SnO_2 samples correspond to the pristine SnO_2 lattice structure (tetragonal, $P4_2/mnm$) [34,35]. From multiple observations of several batches, neither inside structural defects nor any secondary structures were observed, thus indicating that the single crystalline nature of individual grains is well preserved after

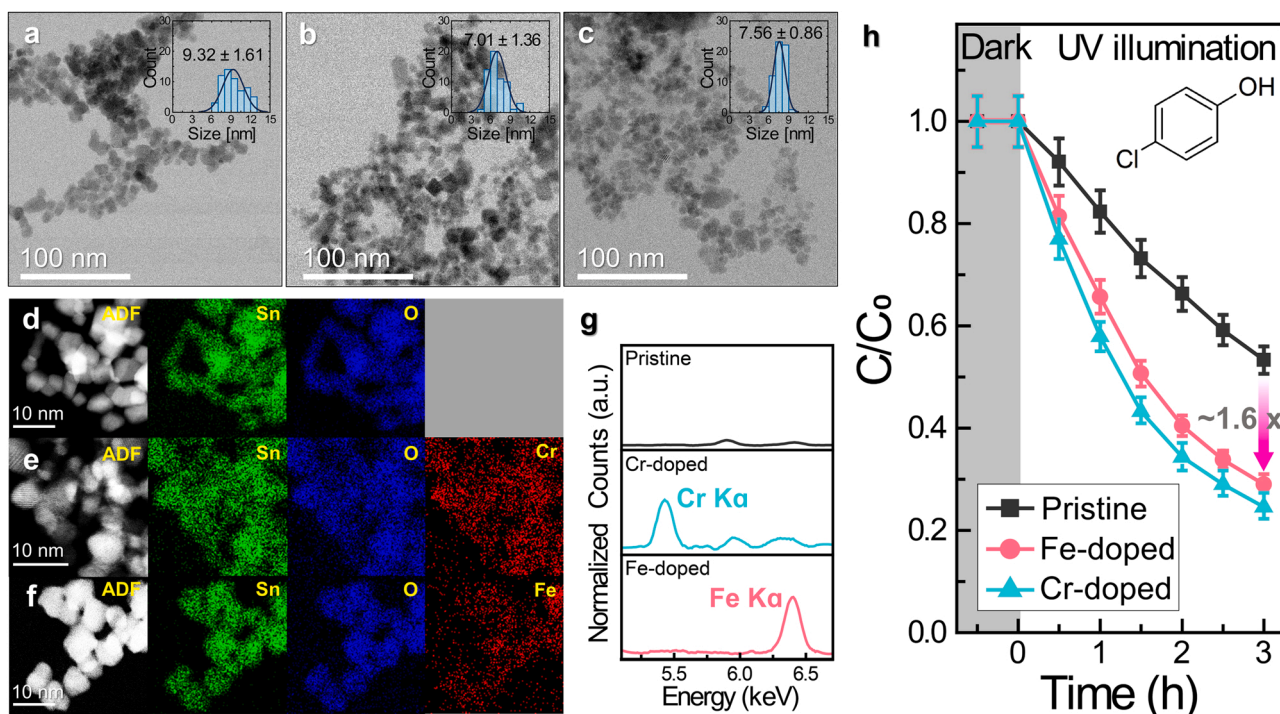


Fig. 1. Morphologies, sizes, and photocatalytic properties of doped SnO_2 NPs. BF-STEM images of (a) pristine, (b) 5 mol% Cr-doped, and (c) 5 mol% Fe-doped SnO_2 NPs annealed at 300 °C. The insets are histograms showing size distributions. The average sizes of the SnO_2 NPs were 9.3 ± 1.6 , 7.0 ± 1.4 , and 7.6 ± 0.9 nm, respectively. Nanoscale elemental mapping for (d) pristine, (e) Cr-, and (f) Fe-doped SnO_2 NPs. Note that all the maps are displayed with image normalization, and thus, the intensities in the maps do not directly indicate the real composition. (g) EDX spectra of the three samples for the energy range of the Fe K_{α} (6.398 kV) and Cr K_{α} (5.411 kV) peaks. (h) Photocatalytic degradation of 4-CP reacted with the three samples under UV irradiation: (black) pristine, (pink) Fe-doped, and (cyan) Cr-doped SnO_2 NPs. Note that a dark process was sustained for the first 30 min before the photocatalytic decomposition reaction by UV irradiation. The degree of 4-CP degradation was estimated by the relation [30]: $\ln(C/C_0) = -k \times t$, where C_0 (mg/L) is the concentration of 4-CP at $t = 0$ min, C (mg/L) is the concentration at a given UV irradiation time, and k is the pseudo-first order rate constant (min^{-1}).

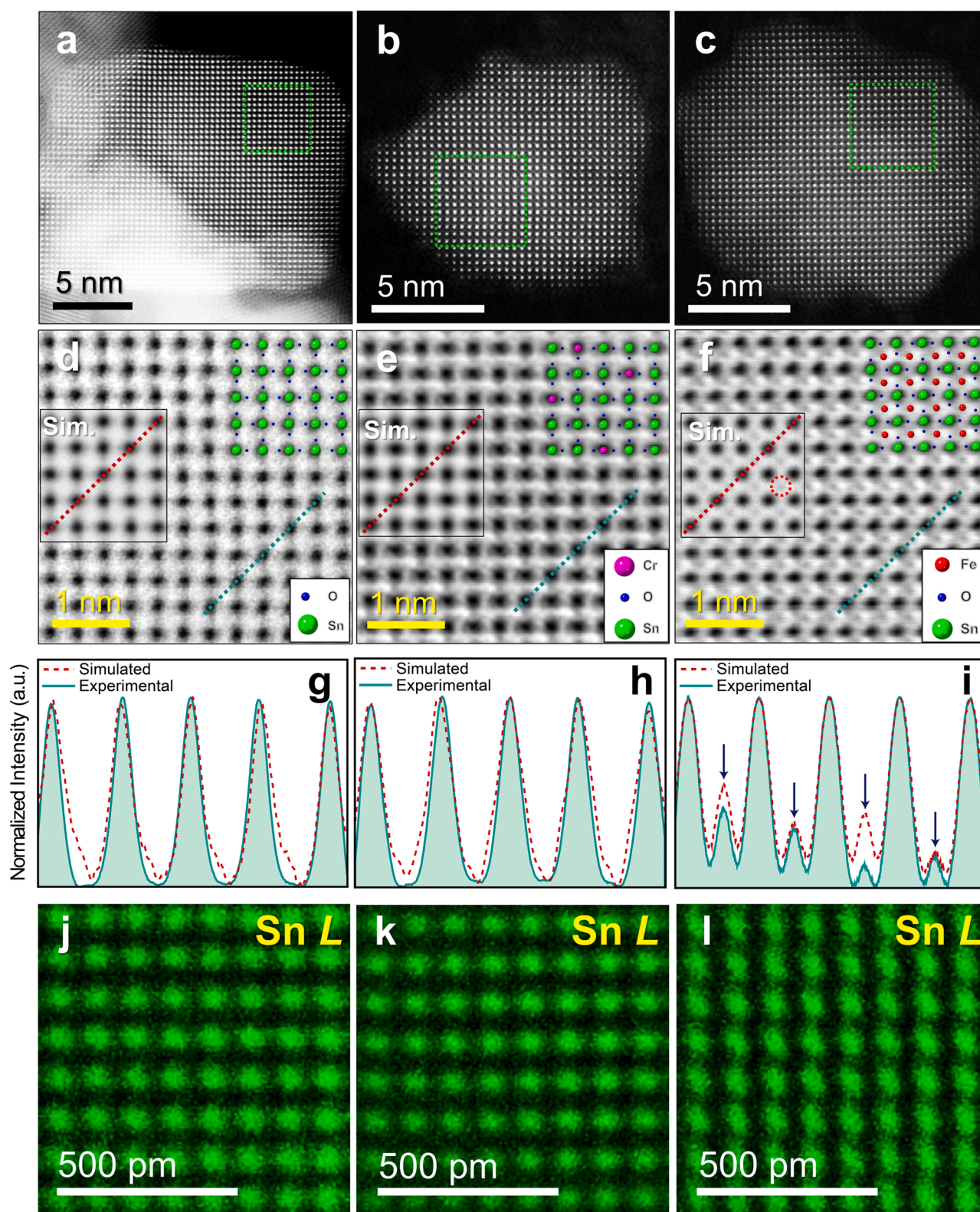


Fig. 2. Atomic-scale imaging and chemical mapping of pristine and doped SnO₂ NPs. (a-c) HAADF STEM images of pristine, Cr-doped, and Fe-doped SnO₂ observed along the [001] orientation. (d-f) High-resolution ABF STEM images of pristine, Cr-doped, and Fe-doped SnO₂ samples. The imaging areas within the SnO₂ NPs are marked by dotted green boxes in the above ADF images. The insets in each figure are the simulated ABF STEM images of the three samples. The corresponding atomic models are superimposed on the experimental images: Sn (green), O (blue), Cr (pink), and Fe (red). (g-i) Comparisons of atomic column-intensity profiles between the simulated (red dotted) and the experimental (green solid) ABF images for the three SnO₂ samples. The profiles correspond to the lines denoted in each ABF image along the [010] direction. (j-l) Atomic-scale EDX maps of Sn L_α (3.604 keV) for pristine, Cr-doped, and Fe-doped SnO₂ NPs.

TM doping. Macroscopic XRD analysis of the three samples shows the same result as the atomic-scale observations (Fig. S2). The three NPs exhibited an irregular shape without developed crystallographic facets. This result implies that no specific crystallographic plane of SnO₂ overwhelmingly contributes to the resulting photocatalytic reaction.

ABF STEM images of the three SnO₂ NPs are displayed in Fig. 2d–f. High-magnification observations of the regions marked by the dotted boxes in the HAADF images were collected (Fig. 2a–c). In this imaging mode, oxygen and a doped element can be imaged when their atomic columns are located in separate locations within the Sn lattice framework. In the ABF image of the Cr-doped SnO₂ NP (Fig. 2e), we observed weak gray contrast only close to the darkest Sn columns, indicating the positions of O; this arrangement of atomic columns is the same as that of the pristine SnO₂ NP (Fig. 2d). This result indicates that the doped Cr atoms substitute for Sn cations (2a Wyckoff position) in the lattice structure. The simulated ABF STEM images of the pristine and Cr-doped SnO₂ structures support our experimental observation (see insets in Fig. 2d, e). In contrast, we intriguingly found that a dark dot in the center of every unit cell is characteristically observed in the ABF STEM image of the Fe-doped SnO₂ NP (Fig. 2f), which is not related to any crystallographic atom sites in the rutile SnO₂ structure but is rather a void site coordinated by six oxygens (4c Wyckoff position). These void positions consequently form a one-dimensional array of interstitial sites along the [001] direction (Fig. S3). Thus, given the noticeable contrast observed in the void sites, we may conclude that doped Fe seems to preferentially populate symmetrical void sites in the SnO₂ structure. Taking the experimental findings into account, the simulated ABF image of the interstitially Fe-doped SnO₂ structure shows a good match with the experimental image (see inset in Fig. 2f). Note that the individual site occupancies of Cr and Fe atoms in the SnO₂ lattice were randomly distributed with a total occupancy of ~0.06 (relative to Sn) to build supercell models for the ABF simulations. The atomic compositions of the Cr-doped and Fe-doped SnO₂ models were Sn₁₅Cr₁O₃₂ and Sn₁₆Fe₁O₃₂, respectively. The assumption of a random occupancy of dopants is reasonable because the intensities observed at interstitial Fe atoms differ from site to site. Profiles of atomic column intensities along the [010] direction (see the dotted lines) clearly show the contrasting doping behaviors of Cr and Fe into SnO₂ NPs; Cr atoms substitute for Sn sites, whereas Fe atoms occupy void sites (Fig. 2g–i). Note that the simulated image showing the best fit to the experimental one for each sample was determined by the cross-correlation analysis (Fig. S4). Complementarily, atomic-scale EDX elemental maps of Sn atoms in the three samples show that all the Sn cations only reside in the assigned 2a Wyckoff position of the rutile SnO₂ structure (Fig. 2j–l). This means that there is no site exchange of Sn atoms with the Fe dopants.

From a simple geometrical consideration, we found that the volume of the oxygen octahedron ($V_{\text{interstitial}} = 13.27 \text{ \AA}^3$) for void sites is larger than that ($V_{\text{substitutional}} = 11.98 \text{ \AA}^3$) of substitutional sites (Fig. S3). The larger volume of voids would facilitate the accommodation of foreign dopants therein. However, the length ($L_{\text{O-O, out-of-plane}} = 3.50 \text{ \AA}$) between apical oxygens in the octahedron is much smaller than that ($L_{\text{O-O, in-plane}} = 4.77 \text{ \AA}$) of equatorial oxygens, whereas the lengths of all oxygens in the octahedron for Sn sites have the same value ($L_{\text{O-O in 2a}} = 4.19 \text{ \AA}$). Given that apical oxygen atoms strongly influence the localization of the in-plane electronic wave function [36], systematic theoretical modeling should be considered to understand the complex interaction of TM dopants and coordinated oxygen atoms, which presumably causes a significant variation in the resulting band structure with doping [37]. In particular, it is worth noting that the stability of doping-mediated electronic reconfiguration is strongly intertwined with lattice distortion [32].

3.3. Lattice strain analysis of Cr- and Fe-doped SnO₂ NPs

Since the XRD results showed no evidence for lattice strain induced by doping (Fig. S2), any strain would be too subtle to be detected due to

the very small doping content. To examine whether the SnO₂ lattice is distorted by doping, the HAADF STEM images were subjected to computational atom position analysis, which enables the statistical estimation of distances between local atomic columns for every unit cell with picometer precision. This approach has been widely used to quantitatively detect subtle changes in the lattice parameters of crystals, and its measurement precision is at the level of ± 3 or 4 pm [38]. Fig. 3 shows the results of unit-cell-specific lattice distortion mapping of the three samples performed along the horizontal direction (corresponding to the fast scan direction of the scanning probe). The false color-coded contrast of each line in the overlapped maps represents the magnitude of the measured Sn–Sn distance ($d_{\text{Sn-Sn}}$), which then spatially displays whether each lattice is expanded or contracted along the measured direction. In the maps and resulting histograms showing the statistical distribution of measured spacings for the pristine and Cr-doped SnO₂ NPs (Fig. 3a, d and b, e, respectively), the average values ($d_{\text{Sn-Sn, p}} = 3.35$ and $d_{\text{Sn-Sn, Cr}} = 3.34 \text{ \AA}$, respectively) were almost identical and corresponded to the typical value of the rutile SnO₂ structure ($d_{\text{Sn-Sn}} = 3.35 \text{ \AA}$). For the case of the Fe-doped SnO₂ NP (Fig. 3c, f), the average measured distance ($d_{\text{Sn-Sn, Fe}} = 3.39 \text{ \AA}$) was slightly larger than those of the other two samples. However, this result seems inconsistent because the difference is at the level of the measurement precision of this approach. To determine whether the difference was a statistical variation or a meaningful value, we compared the extended planar distance accumulated over 20 layers for the three samples, as shown in Fig. 3g. The results reveal that for 20 layers, Fe-doped SnO₂ is slightly expanded by $\sim 37 \text{ pm}$ in comparison to the pristine and Cr-doped samples (see the right graph).

Our DFT calculations accordingly predict the characteristic lattice expansion of SnO₂ by interstitial Fe doping, whereas substitutional Cr doping induces no noticeable change in the lattice. For a $2 \times 2 \times 2$ supercell of SnO₂ with one Fe interstitial, the distance between Sn atoms is significantly expanded by $\sim 10\%$ compared to pristine SnO₂ (Fig. S5a). This notable change should be readily measurable by atomic-scale STEM observation if Fe atoms occupy the interstitial sites in SnO₂ NPs. However, according to the HAADF image simulation of a large supercell containing DFT-derived Fe-doped SnO₂ unit cells that are arbitrarily distributed inside the supercell framework, the lattice distortion induced by Fe doping could become difficult to measure because of the intensity-averaging effect of the mixed (displaced and undistorted) Sn atomic columns in the HAADF image (Fig. S5b). This underestimation is attributed to the practical limitation of our approach, which measures the distances of projected atomic columns instead of true individual bond lengths in the crystal lattice. However, the capability of this approach to detect a subtle lattice distortion with high sensitivity is still useful and valid, given that the statistical histogram obtained from the simulated HAADF image (Fig. S5b) shows excellent consistency with the experimental results (Fig. 3d, f).

3.4. Site-selective doping of Cr and Fe ions in SnO₂ structure

To reveal the origin of the contrasting doping behaviors of Cr and Fe into SnO₂, we investigated the defect formation energies of the substitutional and interstitial sites occupied by Cr and Fe using DFT calculations (Fig. 4a). We found that Cr³⁺ ions preferentially occupy substitutional sites (0.96 eV) with a much lower energy cost than interstitial sites (2.36 eV), whereas Fe³⁺ ions show the opposite trend (3.21 eV for substitutional sites and 2.29 eV for interstitial sites). Rutile SnO₂ is nonstoichiometric with O-related intrinsic defects, consequently introducing shallow donor levels near the conduction band [39]. Mutually interacting with V_O, Sn interstitials are also energetically favorable defects, and their presence synergistically lowers the formation energy of V_O [40]. However, the presence of Sn interstitials in the SnO₂ NPs was not evident from our STEM and EDX measurements. Considering nonstoichiometric SnO₂ with V_O defects, we expect that the amount of V_O would be increased in Cr-doped SnO₂ NPs and

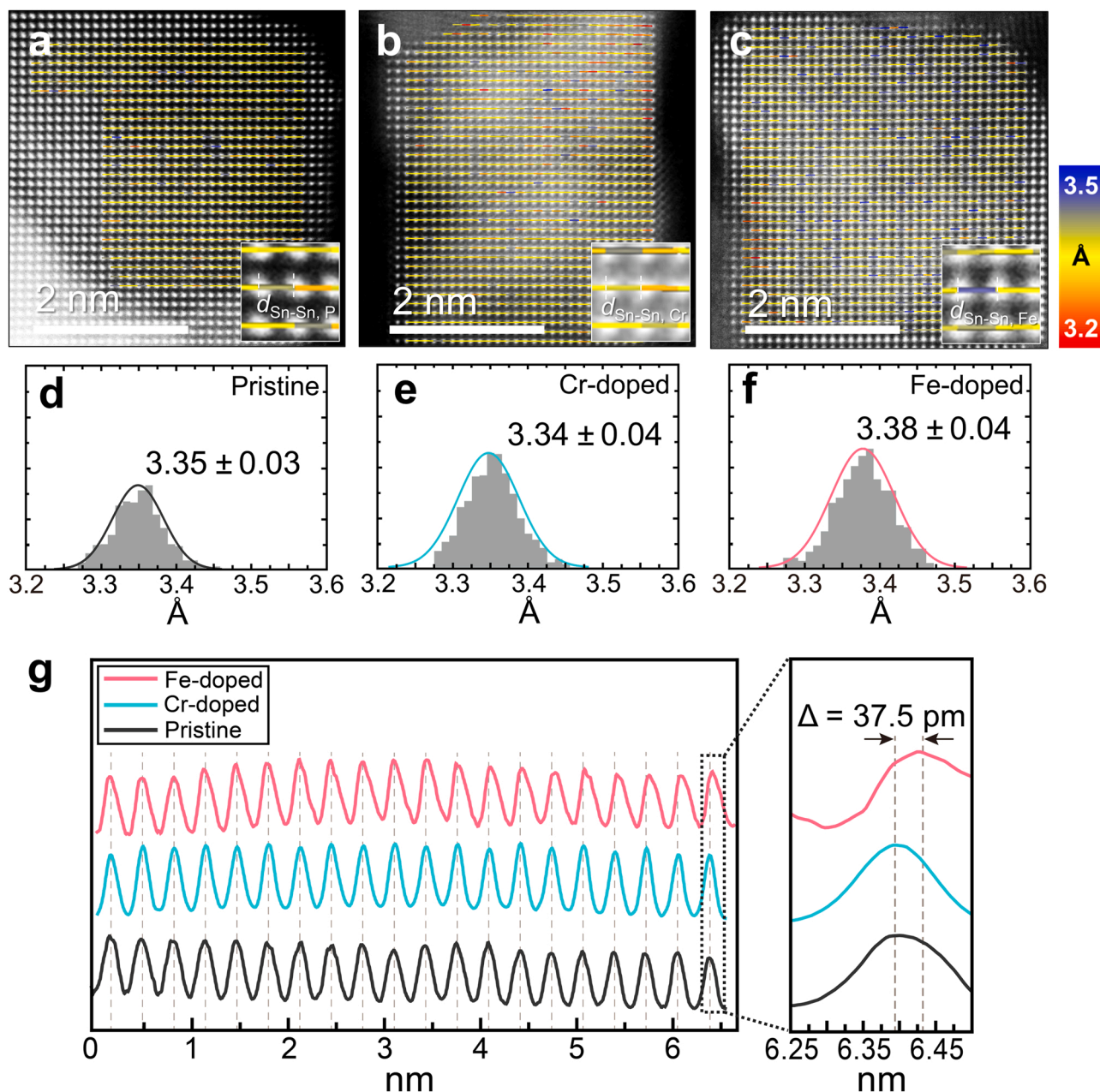


Fig. 3. Quantitative lattice distortion analysis. (a–c) Projected bond length maps overlaid on ADF STEM images of pristine, Cr-doped, and Fe-doped SnO_2 NPs. The distances between two neighboring atoms were measured along the fast scanning-horizontal direction, and the false color in each measured value represents the magnitude of the atomic distance corresponding to the color scale (see the insets). (d–f) Histograms obtained from the projected bond length maps for the three samples. (g) Comparison of intensity profiles of the three SnO_2 NPs obtained for 20 at. columns: pristine (black), Cr-doped (cyan), and Fe-doped (pink) samples.

considerably decreased in Fe-doped SnO_2 NPs compared to that in undoped SnO_2 NPs. This is because the reduced charge state of substitutional Cr^{3+} ions for Sn^{4+} sites requires the formation of V_O acting as electron donors, whereas interstitial Fe^{3+} ions introduce excess electrons, leading to the annihilation of V_O . From the DFT calculations of the V_O formation energies at the surfaces of substitutional Cr-doped and interstitial Fe-doped SnO_2 (Fig. 4b), the V_O formation energy for Cr-doped SnO_2 is decreased by 1.06 eV, while that for Fe-doped SnO_2 is significantly increased by 1.16 eV compared to that for pristine SnO_2 . These results imply that substitutional Cr doping is accompanied by the formation of V_O in SnO_2 NPs, but that interstitial Fe doping shows the opposite trend.

To further confirm this contrasting doping behavior, we performed electron energy loss spectroscopy spectrum imaging (EELS SI) to obtain

the site-specific electron energy loss near edge structure (ELNES) of the O K edge from individual NPs of the three samples. Fig. 4c, e, g displays the chosen regions for analysis (top, green box) and the acquired EELS SI datasets (bottom) for the pristine, Cr-doped, and Fe-doped SnO_2 NPs. From the EELS SI data, we arbitrarily extracted eight O K spectra for the three NPs (numbered 1–8 in each EELS SI dataset), and the O K profiles are displayed in Fig. 4d, f, h. The experimental O K ELNES of SnO_2 exhibits a characteristic doublet peak shape characterized by peaks A (~ 534 eV) and B (~ 540 eV) with an energy difference ($\Delta E_{\text{B-A}}$) of ~ 5.6 eV, which is dominated by the transition to hybridized empty states of O $2p$ or O $2p$ -Sn $5s$ - p orbitals (Fig. S6a) [41,42]. This characteristic peak splitting of O K ELNES was also observed for SnO , but $\Delta E_{\text{B-A}}$ (~ 2.9 eV) is much smaller than that of SnO_2 , and the relative peak intensity of A to B is reversed (Fig. S6b). A previous report showed that a

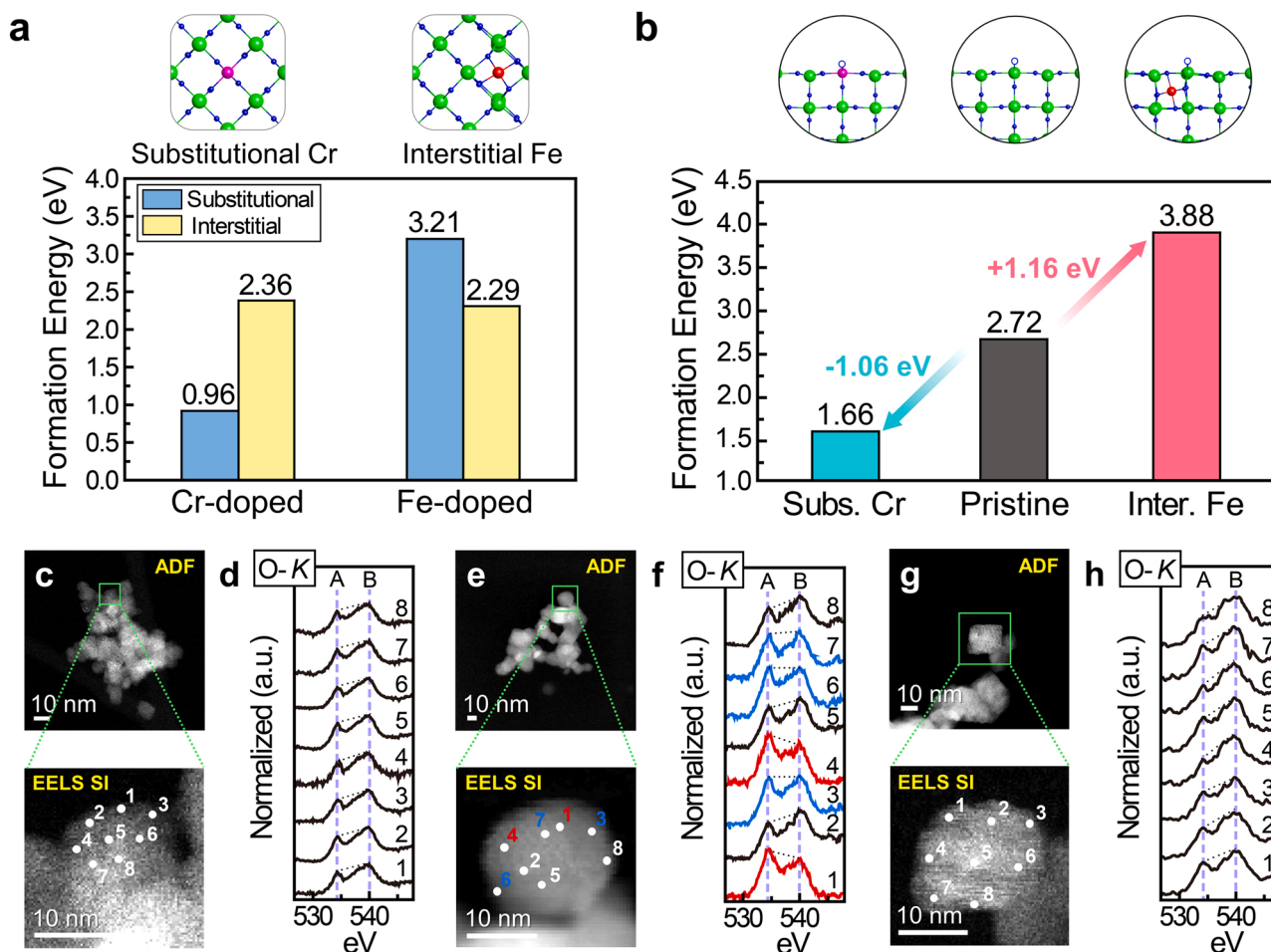


Fig. 4. DFT calculations and EELS analysis. (a) Comparison of formation energies for substitutional (blue) and interstitial (yellow) defects of Cr and Fe in rutile SnO_2 . The atomic models above the graph indicate the energetically favorable site occupation models of Cr (left) and Fe (right) in SnO_2 . (b) Oxygen vacancy (V_o) formation energies at the surface of pristine (gray), substitutional Cr-doped (cyan), and interstitial Fe-doped (pink) SnO_2 slabs. The three surface models for the calculations are displayed above the graph. (c,e,g) Low-magnification ADF-STEM images (upper panel) of pristine, Cr-doped, and Fe-doped SnO_2 NPs and the corresponding EELS spectrum imaging (SI) dataset for the green boxed region (lower panel). (d,f,h) O K ELNES spectra extracted from arbitrary locations (numbered 1–8) within the pristine, Cr-doped, and Fe-doped SnO_2 NPs, respectively. Note that peak A (~ 535 eV) is smaller than peak B (~ 540 eV) in typical O K ELNES (black) for rutile SnO_2 . The deviations in the O K ELNES spectra from the typical values are indicated by blue and red lines: blue for the case of $A \sim B$ and red for $A > B$.

tin oxide with V_o has an intermediate A/B ratio between those of two compounds [41]. From our EELS test with standard SnO_2 and SnO powders, the A/B ratio between SnO_2 and SnO varies from 0.8 to 1.3. From this result, we can qualitatively determine the V_o content at a specific site of a single NP by comparing the experimentally measured A/B ratios based on the values of standard samples. In the extracted O K ELNES profiles of the pristine SnO_2 NP, peak A is smaller than peak B, which is a previously reported typical spectral feature of SnO_2 (Fig. 4d) [41]. However, we noticed a remarkable change in the shape of the O K ELNES profile of the Cr-doped SnO_2 NP compared to the pristine SnO_2 NP (Fig. 4f). Clearly, the height of peak A relative to that of peak B dynamically varies depending on the location. From the eight extracted O K ELNES profiles, we can distinguish three distinct shapes according to the different A/B ratios, which are depicted in black (for $A/B < 1$), blue (for $A/B \sim 1$), and red (for $A/B > 1$). The results suggest that V_o defects are unevenly populated with different concentrations inside the NP. The locations (marked by 1 and 4 in the EELS SI) showing $A/B > 1$ have a high concentration of V_o , while the other locations (marked by 2, 5, and 8) exhibiting $A/B < 1$ have a V_o content similar to that of pristine SnO_2 . Interestingly, an implicative spectral feature is further found in the O K ELNES profiles of Fe-doped SnO_2 (Fig. 4h). The overall spectral shapes appear similar to those of pristine SnO_2 . However, close inspection of the O K ELNES profiles reveals that some of the A peak intensities (denoted

by 2, 4, 6, and 8) are lower than those of pristine SnO_2 , suggesting a suppressed V_o content. This result supports the electron-donating role of interstitial Fe^{3+} ions, as discussed above. It should be noted that all the measured ΔE_{B-A} values for the two doped SnO_2 NPs have the same value as that of pristine SnO_2 , thus meaning that there is no local transition to SnO despite the A/B ratios being similar to or less than that of the reference SnO sample.

3.5. Oxygen vacancy distribution mapping and surface band structures

To examine how the A/B ratio of the O K fine structure in SnO_2 changes in response to variations in V_o concentration, we conducted X-ray absorption near-edge structure (XANES) K-edge simulations for a series of slab models with decreasing oxygen contents starting from $\text{Sn}_{60}\text{O}_{120}$ (stoichiometric) to $\text{Sn}_{60}\text{O}_{110}$ (8.3% deficiency of O) (left, Fig. 5a). Similar to the experimental O K ELNES results, the most distinct spectral change in the XANES O K profiles is the gradual increase in the A/B ratio with increasing V_o content (middle and right, Fig. 5a). As another characteristic, the energy difference (ΔE_{B-A}) remains unchanged at ~ 5.6 eV for the whole range of V_o contents, which is notably consistent with the experimental EELS data. However, the change in the A/B ratio deviates slightly from a linear dependency. This nonlinearity could hinder the absolute estimation of the local V_o content, which

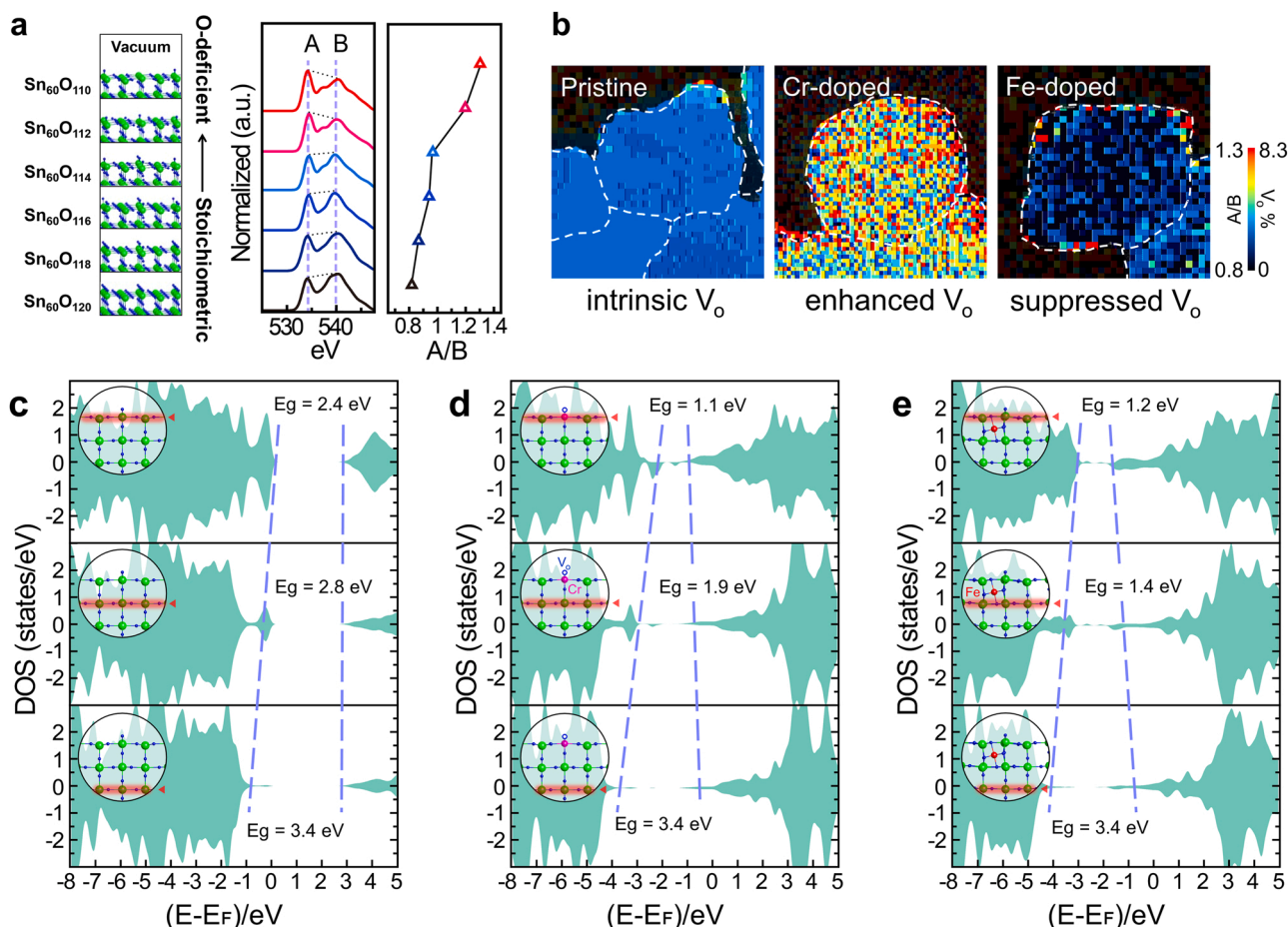


Fig. 5. Oxygen vacancy (V_O) mapping and surface bandgaps. (a) (left) Surface slab models with increasing V_O from SnO_2 to $\text{SnO}_{1.83}$. (middle) X-ray absorption near edge structure (XANES) simulations corresponding to the models. (right) The intensity ratio (A/B) of peak A to peak B from the simulated spectra. (b) V_O maps for the three SnO_2 samples, which were converted from the measured A/B values in the corresponding EELS SI dataset by comparison with the simulated references. The vacuum regions showing meaningless fluctuations in A/B in each V_O map are shaded in gray for clear visualization. Projected density of states (PDOS) of (c) the pristine SnO_2 (110) slab, (d) substitutional Cr-doped SnO_2 (110) slab, and (e) interstitial Fe-doped SnO_2 (110) slab. The PDOS was calculated down to three layers deep from the outermost surface in the slab models. The dotted lines indicate bandgap narrowing when approaching the surface. Bandgap narrowing is more pronounced in Cr-doped and Fe-doped SnO_2 , which suggests that the photocatalytic properties of the doped NPs should be better than that of pristine SnO_2 .

would be further aggravated by other extrinsic factors, such as nonlinear thickness dependence and complex delocalization behavior, that affect the resulting EELS edge intensities [38,43]. Nonetheless, the distinct change in the A/B ratio as a function of local V_O content can be used as a reference indicator to map the spatial distribution of V_O for relative comparison.

Using the simulated O K edges as a reference, we obtained A/B ratio maps of the O K edges extracted from the EELS SI datasets (shown in Fig. 4c, e, g) for the three SnO_2 NPs; these maps are directly related to the distribution of V_O through the entire NP (Fig. 5b). Thus, these A/B maps can be translated into V_O distribution maps, thereby directly visualizing how many V_O defects are spatially distributed throughout the SnO_2 NP. From this mapping technique, we found a clear difference in V_O distribution for the doped SnO_2 NPs. As is well known for SnO_2 , the pristine SnO_2 NP has an intrinsic V_O amount (left, Fig. 5b). However, a large amount of V_O is distributed over the entire Cr-doped SnO_2 NP (middle, Fig. 5b), but the density is more uneven than that of the pristine NP. Further, V_O is apt to be concentrated near the surface (see the red pixels in the V_O map). We expect that the highly localized V_O at the surface of Cr-doped SnO_2 can contribute to enhancing its photocatalytic activity. In contrast, we observe that the V_O concentration is substantially reduced over the entire Fe-doped SnO_2 NP (right, Fig. 5b). This experimental result strongly suggests that Fe interstitials could donate excess electrons into SnO_2 and then annihilate the existing V_O content to

some extent. Therefore, it is presumed that the relatively low photocatalytic performance of Fe-doped SnO_2 NPs originates from the reduction in V_O content due to the presence of Fe interstitials. Macroscopic measurements by X-ray absorption spectroscopy (XAS) confirmed that V_O defects are coupled only with Cr-doped SnO_2 because distinctive defect states in the O K edge were detected only in the Cr-doped sample, not in the pristine and Fe-doped samples (Fig. S7b and Note S1). Additionally, electron spin resonance (ESR) analysis whose signal is attributed to the behavior of unpaired electrons generated by oxygen vacancies under increasing magnetic field showed that the ESR signal is stronger for Cr-doped SnO_2 NPs, whereas it becomes weaker for Fe-doped SnO_2 NPs, as compared to the undoped SnO_2 NPs (Fig. S8). This result is consistent with the results of EELS vacancy distribution mapping.

Since the reduced charge states of TMs doped into SnO_2 NPs are one of the key prerequisites for the interpretation drawn above, we examined the Cr and Fe L edges in the Cr-doped and Fe-doped SnO_2 NPs, respectively, by the EELS SI technique. The shape and position of the TM L edge sensitively vary with the oxidation state and the local bonding environment because the spectral feature originates from the transition of the $2p$ core-level electron to empty $3d$ orbital states. The change in oxidation state of $3d$ metals can be determined by measuring the intensity ratio of the L_3 to L_2 peaks [33,38,44]. The L_3/L_2 ratio maps of Cr and Fe show that both elements have the same oxidation state of +3 in

the SnO₂ NPs (Fig. S9). The local EELS results also correspond to the XAS results for the Cr-doped and Fe-doped SnO₂ powders (Fig. S8c–f).

Our combined atomic-resolution microscopy and spectroscopy results have revealed the site-selective (substitutional and interstitial) doping behaviors of doped Cr and Fe in rutile SnO₂: substitutional Cr³⁺ associated with V_o defects and interstitial Fe³⁺ coupled with lattice strain. In the mesoscopic measurements, however, we witnessed enhanced photocatalytic properties of SnO₂ NPs in both doping cases, although the effect of Fe doping was slightly less than that of Cr doping. To elucidate how substitutional Cr-vacancy cooperation and interstitial Fe-strain coupling change the electronic structure of SnO₂, we performed DFT calculations by considering a 2 × 3 supercell SnO₂ (110) slab consisting of 180 atoms and 5 at. layers. The surface plane of the 2 × 3 supercell SnO₂ (110) slab is composed of 12 Sn and 24 O atoms. The slabs are all set up symmetrically so that the two surfaces of each slab are identical. Due to this mirror symmetry of the slab structure, the projected density of states (PDOS) was plotted from the surface to the third atomic layer (Fig. 5c–e). For the pristine SnO₂ (110) slab, the insulating gap remains unchanged regardless of the surface and bulk-like third atomic layer except for the continuous bandgap narrowing originating from valence band bending (Fig. 5c). In contrast, the substitutional Cr-V_o complex and interstitial Fe produce defect levels in the bandgap and introduce excess electrons, significantly narrowing the bandgap (almost 70% reduction) and shifting the Fermi level up (Fig. 5d, e), which consequently improve the photocatalytic properties in both cases compared to that of pristine NPs. From the UV-Vis absorption measurements (Fig. S10), it is confirmed that the optical bandgaps of the Cr-doped and Fe-doped SnO₂ NPs become indeed narrow to 3.48 and 3.34 eV, respectively, as compared to that of the pristine SnO₂ NPs (3.78 eV). In addition, the deviation from the linearity in the Tauc plots at lower energies is pronounced in the Cr-doped and Fe-doped SnO₂ NPs. This characteristically extended absorbance below the measured bandgap indicates the transitions involving the excitation of electrons from intercalative mid-gap states to the conduction band [45].

4. Conclusions

In summary, we have unveiled the distinct doping behaviors of Cr and Fe ions in the rutile SnO₂ structure, where two crystallographic sites are coordinated by six oxygens: substitutional (2a) and interstitial sites (4c). Atomic-resolution microscopy combined with multiscale spectroscopy and DFT modeling revealed that Cr³⁺ ions prefer substitutional sites, whereas Fe³⁺ ions prefer to occupy interstitial sites. The picoscale lattice distortion analysis showed that interstitial Fe ions induce a lattice strain, while substitutional Cr ions are not involved with lattice strain evolution, but rather coupled with V_o for charge compensation. Our developed V_o distribution mapping approach for a single-particle regime remarkably revealed that the site-specific charge contributions and resulting lattice strains are strongly correlated with the population of V_o. V_o defects tend to be highly concentrated in Cr-doped SnO₂ NPs with segregation at the surface. In contrast, the V_o density in Fe-doped SnO₂ NPs is suppressed compared to that in pristine SnO₂ NPs. This result implies that Cr³⁺ replaces Sn⁴⁺ without the presence of Sn interstitials, while Fe³⁺ additionally enters interstitial sites, which then results in different site-specific doping behaviors by the two dopants. That is, substitutional Cr³⁺ ions replacing Sn⁴⁺ act like a negatively charged p-type dopant requiring V_o. In contrast, interstitial Fe³⁺ ions play the role of a positively charged n-type dopant emitting excess electrons. Both cases can generate a high density of mid-gap states at the surface of SnO₂, which consequently accelerates the photocatalytic activity of the material. Our results provide a clear perspective of the roles of site-selective dopants in the resulting physical properties and convey deeper insight into the atomic-scale doping mechanisms used to develop precise and efficient doping engineering for high-performance MO catalysts.

CRediT authorship contribution statement

Woo-Sung Jang: Investigation, Validation, Writing – original draft. **Yeongrok Jin:** Investigation, Calculation, Writing – original draft. **Young-Hoon Kim:** Investigation, Validation. **Sang-Hyeok Yang:** Investigation. **Seon Je Kim:** Investigation. **Jung A. Hong:** Investigation. **Jaeyoon Baik:** Investigation. **Jaekwang Lee:** Supervision, Calculation, Funding acquisition, Writing – review & editing. **Hangil Lee:** Supervision, Investigation, Funding acquisition, Writing – review & editing. **Young-Min Kim:** Supervision, Investigation, Funding acquisition, Writing – review & editing.

Declaration of Competing Interest

The authors declare that they have no known competing financial interests or personal relationships that could have appeared to influence the work reported in this paper.

Acknowledgments

W.-S.J., Y.R.J., and Y.-H.K. contributed equally to this work. Y.-M.K. acknowledges the support of a National Research Foundation of Korea (NRF) grant funded by the Korean government (NRF-2020R1A2C1006207) and a Technology Innovation Program (No. 20011712) funded by the Ministry of Trade, Industry & Energy (MOTIE, Korea). H.L. acknowledges the support of an NRF grant funded by the Korean government (NRF-2021R1A2C2007992). J.L. acknowledges the support of an NRF grant funded by the Korean government (NRF-2018R1A2B6004394). This work was also supported by the Institute for Basic Science (IBS-R011-D1), Ministry of Science and ICT (MSIT) and Pohang Accelerator Laboratory (PAL) in South Korea.

Appendix A. Supporting information

Supplementary data associated with this article can be found in the online version at doi:10.1016/j.apcatb.2022.121083.

References

- [1] A.V. Nikam, B.L.V. Prasad, A.A. Kulkarni, Wet chemical synthesis of metal oxide nanoparticles: a review, *Crystengcomm* 20 (2018) 5091–5107.
- [2] A.A. AbdelHamid, Y. Yu, J. Yang, J.Y. Yang, Generalized synthesis of metal oxide nanosheets and their application as Li-ion battery anodes, *Adv. Mater.* 29 (2017), 1701427.
- [3] S. Kattel, P. Liu, J.G. Chen, Tuning selectivity of CO₂ hydrogenation reactions at the metal/oxide interface, *J. Am. Chem. Soc.* 139 (2017) 9739–9754.
- [4] A. Tricoli, M. Graf, S.E. Pratsinis, Optimal doping for enhanced SnO₂ sensitivity and thermal stability, *Adv. Funct. Mater.* 18 (2008) 1969–1976.
- [5] B. Tu, Y. Shao, W. Chen, Y. Wu, X. Li, Y. He, J. Li, F. Liu, Z. Zhang, Y. Lin, X. Lan, L. Xu, X. Shi, A.M.C. Ng, H. Li, L.W. Chung, A.B. Djurišić, Z. He, Novel molecular doping mechanism for n-doping of SnO₂ via triphenylphosphine oxide and its effect on perovskite solar cells, *Adv. Mater.* 31 (2019), 1805944.
- [6] Y. Gun, G.Y. Song, V.H.V. Quy, J. Heo, H. Lee, K.-S. Ahn, S.H. Kang, Joint effects of photoactive TiO₂ and fluoride-doping on SnO₂ inverse opal nanoarchitecture for solar water splitting, *ACS Appl. Mater. Interfaces* 7 (2015) 20292–20303.
- [7] L. Yang, J. Huang, L. Shi, L. Cao, H. Liu, Y. Liu, Y. Li, H. Song, Y. Jie, J. Ye, Sb doped SnO₂-decorated porous g-C₃N₄ nanosheet heterostructures with enhanced photocatalytic activities under visible light irradiation, *Appl. Catal. B Environ.* 221 (2018) 670–680.
- [8] R. Xie, X. Meng, P. Sun, J. Niu, W. Jiang, L. Bottomley, D. Li, Y. Chen, J. Crittenden, Electrochemical oxidation of ofloxacin using a TiO₂-based SnO₂-Sb/polytetrafluoroethylene resin-PbO₂ electrode: reaction kinetics and mass transfer impact, *Appl. Catal. B Environ.* 203 (2017) 515–525.
- [9] B. Zhang, Z. Guo, Z. Zuo, W. Pan, J. Zhang, The ensemble effect of nitrogen doping and ultrasmall SnO₂ nanocrystals on graphene sheets for efficient electroreduction of carbon dioxide, *Appl. Catal. B Environ.* 239 (2018) 441–449.
- [10] T. Cao, T. Xia, L. Zhou, G. Li, X. Chen, H. Tian, J. Zhao, J.-O. Wang, W. Zhang, S. Li, S. Meng, H. Guo, Distribution and concentration of surface oxygen vacancy of TiO₂ and its photocatalytic activity, *J. Phys. D Appl. Phys.* 53 (2020), 424001.
- [11] Y.M. Kim, K.H. Lee, L. Fu, M.W. Oh, S.H. Yang, S. Ning, G. Han, M.Y. Kim, J.S. Kim, M. Jeong, J. Jang, E. Lee, E. Okunishi, H. Sawada, Si Kim, S.J. Pennycook, Y.H. Lee, S.W. Kim, Atomic-scale chemical mapping of copper dopants in Bi₂Te_{2.7}Se_{0.3} thermoelectric alloy, *Mater. Today Phys.* 17 (2021), 100347.

- [12] Y.-H. Kim, S. Kim, K.-J. Kim, C. Kim, J.H. Jang, Y.-M. Kim, H. Lee, Multiscale probing of the influence of the defect-induced variation of oxygen vacancies on the photocatalytic activity of doped ZnO nanoparticles, *J. Mater. Chem. A* 8 (2020) 25345–25354.
- [13] J.A. Toledo-Antonio, R. Gutiérrez-Baez, P.J. Sebastian, A. Vázquez, Thermal stability and structural deformation of rutile SnO₂ nanoparticles, *J. Solid State Chem.* 174 (2003) 241–248.
- [14] H.-C. Chiu, C.-S. Yeh, Hydrothermal synthesis of SnO₂ nanoparticles and their gas-sensing of alcohol, *J. Phys. Chem. C* 111 (2007) 7256–7259.
- [15] S.A. Arote, V. Tabhane, S.D. Gunjal, K.C. Mohite, H. Pathan, Structural and optical properties of electrodeposited porous SnO₂ films: effect of applied potential and post deposition annealing treatment, *Macromol. Symp.* 347 (2015) 75–80.
- [16] Q. Jiang, X. Zhang, J. You, SnO₂: a wonderful electron transport layer for perovskite solar cells, *Small* 14 (2018), 1801154.
- [17] L. Xiong, Y. Guo, J. Wen, H. Liu, G. Yang, P. Qin, G. Fang, Review on the application of SnO₂ in perovskite solar cells, *Adv. Funct. Mater.* 28 (2018), 1802757.
- [18] Z. Liu, D.D. Sun, P. Guo, J.O. Leckie, An efficient bicomponent TiO₂/SnO₂ nanofiber photocatalyst fabricated by electrospinning with a side-by-side dual spinneret method, *Nano Lett.* 7 (2007) 1081–1085.
- [19] L. Zheng, Y. Zheng, C. Chen, Y. Zhan, X. Lin, Q. Zheng, K. Wei, Facile one-pot synthesis of ZnO/SnO₂ heterojunction photocatalysts with excellent photocatalytic activity and photostability, *ChemPlusChem* 77 (2012) 217–223.
- [20] Q. Kuang, C. Lao, Z.L. Wang, Z. Xie, L. Zheng, High-sensitivity humidity sensor based on a single SnO₂ nanowire, *J. Am. Chem. Soc.* 129 (2007) 6070–6071.
- [21] H. Zhu, Q. Li, Y. Ren, Q. Gao, J. Chen, N. Wang, J. Deng, X. Xing, A. New, Insight into cross-sensitivity to humidity of SnO₂ sensor, *Small* 14 (2018), 1703974.
- [22] J. Chen, M. Yao, X. Wang, Investigation of transition metal ion doping behaviors on TiO₂ nanoparticles, *J. Nanopart. Res.* 10 (2008) 163–171.
- [23] K. Nomura, C.A. Barrero, J. Sakuma, M. Takeda, Room-temperature ferromagnetism of sol-gel-synthesized Sn_{1-x}Fe_xO_{2-δ} powders, *Phys. Rev. B* 75 (2007), 184411.
- [24] R. Shannon, Revised effective ionic radii and systematic studies of interatomic distances in halides and chalcogenides, *Acta Crystallogr. Sect. A* 32 (1976) 751–767.
- [25] D. Misra, S.K. Yadav, Prediction of site preference of implanted transition metal dopants in rock-salt oxides, *Sci. Rep.* 9 (2019) 12593.
- [26] P.E. Blöchl, O. Jepsen, O.K. Andersen, Improved tetrahedron method for Brillouin-zone integrations, *Phys. Rev. B* 49 (1994) 16223–16233.
- [27] J.P. Perdew, K. Burke, M. Ernzerhof, Generalized gradient approximation made simple, *Phys. Rev. Lett.* 77 (1996) 3865–3868.
- [28] G. Kresse, J. Furthmüller, Efficient iterative schemes for ab initio total-energy calculations using a plane-wave basis set, *Phys. Rev. B* 54 (1996) 11169–11186.
- [29] F. Karsai, M. Humer, E. Flage-Larsen, P. Blaha, G. Kresse, Effects of electron-phonon coupling on absorption spectrum: K edge of hexagonal boron nitride, *Phys. Rev. B* 98 (2018) 235205.
- [30] M.M. Ba-Abbad, A.A.H. Kadhum, A.B. Mohamad, M.S. Takriff, K. Sopian, Photocatalytic degradation of chlorophenols under direct solar radiation in the presence of ZnO catalyst, *Res. Chem. Intermed.* 39 (2013) 1981–1996.
- [31] Y.-M. Kim, S.J. Pennycook, A.Y. Borisevich, Quantitative comparison of bright field and annular bright field imaging modes for characterization of oxygen octahedral tilts, *Ultramicroscopy* 181 (2017) 1–7.
- [32] Y.-M. Kim, A. Morozovska, E. Eliseev, M.P. Oxley, R. Mishra, S.M. Selbach, T. Grande, S.T. Pantelides, S.V. Kalinin, A.Y. Borisevich, Direct observation of ferroelectric field effect and vacancy-controlled screening at the BiFeO₃/La_{0.5}Sr_{0.5}MnO₃ interface, *Nat. Mater.* 13 (2014) 1019–1025.
- [33] J.-H. Shim, Y.-H. Kim, H.-S. Yoon, H.-A. Kim, J.-S. Kim, J. Kim, N.-H. Cho, Y.-M. Kim, S. Lee, Hierarchically structured core-shell design of a lithium transition-metal oxide cathode material for excellent electrochemical performance, *ACS Appl. Mater. Interfaces* 11 (2019) 4017–4027.
- [34] N. Lu, Q. Wan, J. Zhu, Surface structure of zigzag SnO₂ nanobelts, *J. Phys. Chem. Lett.* 1 (2010) 1468–1471.
- [35] H. Matsuhata, J. Gjønnes, J. Taftø, A study of the structure factors in rutile-type SnO₂ by high-energy electron diffraction, *Acta Crystallogr. Sect. A* 50 (1994) 115–123.
- [36] Y.Y. Peng, G. Dellea, M. Minola, M. Conni, A. Amorese, D. Di Castro, G.M. De Luca, K. Kummer, M. Salluzzo, X. Sun, X.J. Zhou, G. Balestrino, M. Le Tacon, B. Keimer, L. Braicovich, N.B. Brookes, G. Ghiringhelli, Influence of apical oxygen on the extent of in-plane exchange interaction in cuprate superconductors, *Nat. Phys.* 13 (2017) 1201–1206.
- [37] L.F. Feiner, M. Grilli, C. Di Castro, Apical oxygen ions and the electronic structure of the high-T_c cuprates, *Phys. Rev. B* 45 (1992) 10647–10669.
- [38] Y.-M. Kim, J. He, M.D. Biegalski, H. Ambaye, V. Lauter, H.M. Christen, S. T. Pantelides, S.J. Pennycook, S.V. Kalinin, A.Y. Borisevich, Probing oxygen vacancy concentration and homogeneity in solid-oxide fuel-cell cathode materials on the subunit-cell level, *Nat. Mater.* 11 (2012) 888–894.
- [39] I.A. Alagdal, A.R. West, Oxygen non-stoichiometry, conductivity and gas sensor response of SnO₂ pellets, *J. Mater. Chem. A* 3 (2015) 23213–23219.
- [40] Ç. Kılıç, A. Zunger, Origins of coexistence of conductivity and transparency in SnO₂, *Phys. Rev. Lett.* 88 (2002), 095501.
- [41] M.S. Moreno, R.F. Egerton, P.A. Midgley, Differentiation of tin oxides using electron energy-loss spectroscopy, *Phys. Rev. B* 69 (2004), 233304.
- [42] M.S. Moreno, R.F. Egerton, J.J. Rehr, P.A. Midgley, Electronic structure of tin oxides by electron energy loss spectroscopy and real-space multiple scattering calculations, *Phys. Rev. B* 71 (2005), 035103.
- [43] M.P. Oxley, S.J. Pennycook, Image simulation for electron energy loss spectroscopy, *Micron* 39 (2008) 676–684.
- [44] G.A. Botton, C.C. Appel, A. Horsewell, W.M. Stobbs, Quantification of the EELS near-edge structures to study Mn doping in oxides, *J. Microsc.* 180 (1995) 211–216.
- [45] C.C. Milleville, K.E. Pelcher, M.Y. Sfeir, S. Banerjee, D.F. Watson, Directional charge transfer mediated by mid-gap states: a transient absorption spectroscopy study of CdSe quantum dot/ β -Pb_{0.33}V₂O₅ heterostructures, *J. Phys. Chem. C* 120 (2016) 5221–5232.